frontiers in Chemistry

ORIGINAL RESEARCH
published: 18 May 2018
doi: 10.3389/fchem.2018.00175

# Photocatalytic Oxidation of Acetone Over High Thermally Stable $TiO_2$ Nanosheets With Exposed (001) Facets

*Ting Shi[1], Youyu Duan[1], Kangle Lv[1]*, Zhao Hu[1], Qin Li[1], Mei Li[1]* and Xiaofang Li[1,2]*

[1] Key Laboratory of Catalysis and Materials Science of the State Ethnic Affairs Commission & Ministry of Education, Hubei Province, College of Resources and Environmental Science, South-Central University for Nationalities, Wuhan, China,
[2] College of Chemistry and Chemical Engineering, Wuhan University of Science and Technology, Wuhan, China

Anatase $TiO_2$ (A-$TiO_2$) usually exhibits superior photocatalytic activity than rutile $TiO_2$ (R-$TiO_2$). However, the phase transformation from A-$TiO_2$ to R-$TiO_2$ will inevitably happens when the calcination temperature is up to 600°C, which hampers the practical applications of $TiO_2$ photocatalysis in hyperthermal situations. In this paper, high energy faceted $TiO_2$ nanosheets ($TiO_2$-NSs) with super thermal stability was prepared by calcination of $TiOF_2$ cubes. With increase in the calcination temperature from 300 to 600°C, $TiOF_2$ transforms into $TiO_2$ hollow nanoboxes ($TiO_2$-HNBs) assembly from $TiO_2$-NSs via Ostwald Rippening process. Almost all of the $TiO_2$-HNBs are disassembled into discrete $TiO_2$-NSs when calcination temperature is higher than 700°C. Phase transformation from A-$TiO_2$ to R-$TiO_2$ begins at 1000°C. Only when the calcination temperature is higher than 1200°C can all the $TiO_2$-NSs transforms into R-$TiO_2$. The 500°C-calcined sample (T500) exhibits the highest photoreactivity toward acetone oxidation possibly because of the production of high energy $TiO_2$-NSs with exposed high energy (001) facets and the surface adsorbed fluorine. Surface oxygen vacancy, due to the heat-induced removal of surface adsorbed fluoride ions, is responsible for the high thermal stability of $TiO_2$-NSs which are prepared by calcination of $TiOF_2$ cubes.

**Keywords: $TiO_2$, photocatalytic degradation, acetone, fluorine, oxygen vacancy**

OPEN ACCESS

***Edited by:***
*Fan Dong,*
*Chongqing Technology and Business University, China*

***Reviewed by:***
*Xin Li,*
*South China Agricultural University, China*
*Shiyong Sun,*
*Southwest University of Science and Technology, China*

****Correspondence:***
*Kangle Lv*
*lvkangle@mail.scuec.edu.cn*
*Mei Li*
*limei@mail.scuec.edu.cn*

***Specialty section:***
*This article was submitted to Catalysis and Photocatalysis, a section of the journal Frontiers in Chemistry*

***Received:*** *07 April 2018*
***Accepted:*** *30 April 2018*
***Published:*** *18 May 2018*

***Citation:***
*Shi T, Duan Y, Lv K, Hu Z, Li Q, Li M and Li X (2018) Photocatalytic Oxidation of Acetone Over High Thermally Stable $TiO_2$ Nanosheets With Exposed (001) Facets. Front. Chem. 6:175. doi: 10.3389/fchem.2018.00175*

## INTRODUCTION

Semiconductor photocatalysis has attracted much attention due to its potential applications such as water (Regmi et al., 2018; Xu et al., 2018) and air purification (Wen et al., 2015; Cui et al., 2017; Li et al., 2017a; Qi et al., 2017) and water splitting for clean $H_2$ energy (Cheng et al., 2018) due to its peculiar chemical and physical properties. As a typical semiconductor photocatalyst, anatase $TiO_2$ (A-$TiO_2$) usually shows excellent photocatalytic activity. However, it usually transforms into poor photoreactive rutile $TiO_2$ (R-$TiO_2$) when calcination temperature is higher than about 600°C, which hampers the practical applications of A-$TiO_2$ in hyperthermal situations (Lv et al., 2011; Liang et al., 2017). For example, the temperature of some industrial waste gases after burning can be as high as 900–1000°C, which makes the photocatalytic oxidation technology lose its power due to the phase transformation of A-$TiO_2$ at such high temperature. There are many photocatalytically active stable $TiO_2$-coated ceramic materials which are used for the control of organic contaminants,

including sanitary wares, bathroom tiles and self-cleaning glass. They require high processing temperatures and therefore need excellent stability at high temperature (Periyat et al., 2009). Thus, exploration of thermally stable $TiO_2$ photocatalyst is very important but this question remains unsolved.

As one of volatile organic compounds (VOCs), acetone is a widely used solvent especially in chemical plant. The emission of acetone can not only cause the problems to global environment, but also bring harms to human health (Zhu et al., 2016). When the concentration of acetone vapor is higher than 500 ppm, it can irritate eyes and discomfort respiratory system (Li et al., 2018). So, it is of great importance to explore an efficient method to decompose of acetone. Because semiconductor photocatalysis is considered as an environmentally benign way, it is no doubt very promising for VOCs removal under normal conditions.

It is generally accepted that the quantum efficiency of photocatalysis is highly related to the physical properties of $TiO_2$ such as crystal structure, relative crystallinity, size of the particle, and specific surface area (Xu et al., 2007; Lan et al., 2015; Wang et al., 2015, 2016; Wen et al., 2015; Li et al., 2016; Sajan et al., 2016; Liang et al., 2017; Xia et al., 2017; Lin et al., 2018a,b). Recently, growing interesting has been devoted to the synthesis of $TiO_2$ nanocrystals with exposed high energy {001} facets by surface fluorination of $TiO_2$ to reduce the surface energy (Yang et al., 2008, 2009; Chen et al., 2010; Yu et al., 2014; Sajan et al., 2016; Liang et al., 2017). On considering that $TiOF_2$ cubes are fluorine-containing materials, they prefer to transform into high energy $TiO_2$ nanocrystals during calcination. After the removal of surface adsorbed fluorine ions at high temperature, the formed oxygen vacancy (OV) on the surface of the photocatalyst will prevent the fusion of neighboring A-$TiO_2$ nanocrystals, which is believed to improve the thermal stability of $TiO_2$ nanocrystals. Herein, we systematically studied the dependence of the structure and photocatalytic activity of $TiOF_2$ cubes on the calcination temperature. Acetone was selected as the targeted VOCs to evaluate the photoreactivity of the as-prepared photocatalyst.

# EXPERIMENTAL SECTION

## Synthesis

Precursor $TiOF_2$ was synthesized through the solvothermal reaction of Tetrabutyl titanium (TBT), acetic acid (HAc) and hydrofluoric acid (HF) (Huang et al., 2013). Typically, 20.0 g of TBT was dropwise added into the mixed solution containing 6.4 ml of HF (47 wt%) and 40.0 ml of HAc under magnetic stirring. The resulted white suspensions were transferred to an autoclave with volume of 100 ml, which was then kept at 200°C for 2 h. The white deposition was collected and washed with ethanol and distilled water until the filtrate is neutral (pH7). After oven dry at 80°C, we obtained the precursor $TiOF_2$.

Precursor $TiOF_2$ was then calcined at certain temperature (300-1200°C) for 2 h by keeping the same heating rate (5°C $min^{-1}$). The obtained photocatalyst is denoted as Tx (**Table 1**), where x is the calcination temperature. For example, T500 is that the photocatalyst which was prepared by calcination of the precursor $TiOF_2$ at 500°C for 2 h.

**TABLE 1** | Physical property of the photocatalyst.

| Sample | Calcination temperature (°C) | Phase structure[a] | $S_{BET}$[b] ($m^2g^{-1}$) |
|---|---|---|---|
| T300 | 300 | $TiOF_2$ | 5.7 |
| T400 | 400 | $TiOF_2$/A-$TiO_2$ | 6.4 |
| T500 | 500 | $TiOF_2$/A-$TiO_2$ | 5.6 |
| T600 | 600 | A-$TiO_2$ | 3.2 |
| T700 | 700 | A-$TiO_2$ | 2.4 |
| T800 | 800 | A-$TiO_2$ | 2.0 |
| T900 | 900 | A-$TiO_2$ | 2.0 |
| T1000 | 1000 | A-$TiO_2$/R-$TiO_2$ | 1.3 |
| T1100 | 1100 | A-$TiO_2$/R-$TiO_2$ | 1.2 |
| T1200 | 1200 | R-$TiO_2$ | 0.4 |

[a] *A-$TiO_2$ and R-$TiO_2$ represent anatase $TiO_2$ and rutile $TiO_2$, respectively.*
[b] *The BET surface area is determined by a multipoint BET method using the adsorption data in the relative pressure ($P/P_0$) range from 0.05 to 0.3.*

## Characterization

XRD patterns of the photocatalysts were performed on a X-ray diffractometer (D8- advance, Bruker Co., German), and the scan rate of Cu K*a* radiation keeps 0.02° 2θ $s^{-1}$, using an accelerated voltage and applied current of 15 kV and 20 mA, respectively. We observe the morphology of the prepared photocatalyst by an FESEM with an acceleration voltage of 20 kV (Hitach, Japan) and a TEM (Tecnai G20, USA) using an acceleration voltage of 200 kV, respectively. The optical property of the photocatalyst was measured by a spectrophotometer (UV-2550, Shimadzu, Japan) from 200 to 800 nm using $BaSO_4$ as background. FTIR was obtained on a infrared spectrometer (NeXUS 470) using the KBr pellet technique. XPS was recorded using monochromatic Al-Ka radiation under vacuum at $2 \times 10^{-6}$ Pa on a photoelectron spectrometer (VG Multilab 2000). The C1s peak at 284.8 eV originated from the surface adventitious carbon is used to reference all the binding energies. EPR signal of the photocatalyst was recorded in an EPR spectrometer (JES-FA 200, JEOL) at room temperature (frequency of 100 kHz and microwave power of 0.99 mW). Nitrogen sorption isotherm was measured on an ASAP 2020 nitrogen adsorption equipment (Micromeritics, USA). Before investigating the surface areas of the photocatalysts, all samples were degassed firstly at 200°C.

## Photoelectrochemical Measurements

We use CHI760e as electrochemical workstation (Shanghai, China) to measure the transient photocurrent, EIS Nyquist plots and Mott-Schottky plots in a standard there-electrode system, where Pt wire was used as the counter electrode, and the prepared samples and Ag/AgCl in saturated KCl were used as the working and reference electrode, respectively. During the measurement, 0.4 M $Na_2SO_4$ was used as electrolyte solution. In the Mott-Schottky measurement, direct current potential polarization was kept at a fixed frequency, and the working electrode was prepared on a glassy carbon electrode. Before the test of photocurrent, 50 mg photocatalysts and 30 μL Nafion were dispersed into 1 mL water/absolute ethanol mixed solvent (v/v = 1/1), and then the mixed aqueous solution was dispersed uniformly

through ultrasound to form a homogeneous catalyst colloid. The ITO/$TiO_2$ electrode was prepared using the as-prepared photocatalyst colloid as precursor by a drip coating method. The light source is a 3W LED lamp (Shenzhen LAMPLIC, China) emitted mainly at 365 nm. The intensity for the lamp at working distance is measured to be 0.41 W/$cm^2$.

## Evaluation of the Photocatalytic Activity

Photocatalytic oxidation of gasous acetone was used to evaluate the photocatalytic activity of the photocatalyst, which was performed in a 15 L reactor at ambient temperature under UV light irradiation. 0.3 g of the powder was firstly dispersed in 30 mL of double distilled water by sonicating treatment for 5 min. The obtained suspensions were then evenly transferred into three glass dishes in diameters of about 7.0 cm. After drying at 80°C for about 2 h, the dishes that have been coated with a layer of the photocatalyst were placed in the reactor, and then 10 uL of acetone was injected into the reactor by a microsyringe. The vaporated acetone then begins to adsorb on the surface of the photocatalyst. Thirty minutes later, the adsorption–desorption equilibrium of acetone can be established. The photocatalytic oxidation of acetone begins after turning on the UV light, which is 5 cm above the dishes. The concentrations of acetone and the produced carbon dioxide in the reactor were determined online with a Photoacoustic IR Multigas Monitor (Model 1412, INNOVA). Before irradiation, the initial concentration of acetone after the adsorption equilibrium was about 300 ppm, which almost keeps unchanged for about 5 min before lighting a UV lamp (15W@365 nm).

# RESULTS AND DISCUSSION

## Effect of Calcination Temperature on Phase Structure

Phase structure of the photocatalyst is important to the photoreactivity. Therefore, we used XRD to study the phase evolution of the photocatalyst during calcination. From **Figure 1**, a broad peak centering at $2\theta = 23.4°$, which corresponds to the (100) plane diffraction of $TiOF_2$, was observed for the prepared precursor, and no any peak of $TiO_2$ phases (A-$TiO_2$ and R-$TiO_2$) exists, indicating the successful synthesis of $TiOF_2$(Huang et al., 2013). After calcination at 300°C for 2 h, the phase struccture of the sample (T300) almost keeps unchanged. With increase in the calcination temperature to 400°C, the peak intensity for $TiOF_2$ decreases. Simultaneously, a small peak at $2\theta = 25.3°$, which corresponds to the (101) plane diffraction of A-$TiO_2$, can be observed for T400 sample, indicating that phase transformation from $TiOF_2$ to anatase begins. This phase transformation becomes obvious after calcination of $TiOF_2$ at 500°C, and the prepared $TiOF_2$ totally transforms into anatase $TiO_2$ at 600°C.

It is proposed that the reaction for the heat-induced phase transformation from $TiOF_2$ to $TiO_2$ is as follows (Equation 1) (Zhao et al., 2018).

$$2TiOF_2 + \text{heat} \rightarrow TiO_2 + TiF_4\uparrow \quad (1)$$

Further increase in the calcination from 600 to 900°C, the peak intensity of A-$TiO_2$ increases, indicating the enhanced crystallization. Meanwhile, the narrowing of the width for the (101) plane diffraction peak indicates the increase of A-$TiO_2$ crystallite size. The peak intensity for the (101) peak of anatase $TiO_2$ begins to decrease at calcination temperature of 1000°C, which is a sign of anatase-to-rutile phase transfermation. The formation of rutile phase is confirmed from the XRD pattern of the T1100 sample due to the formation of a small peak at $2\theta = 27.3°$, which corresponds to the (110) plane diffraction of R-$TiO_2$. Only when the calcination temperature reaches 1200°C can all of the A-$TiO_2$ transform into R-$TiO_2$.

Usually, A-$TiO_2$ nanocrystals begin transform into R-$TiO_2$ at about 600°C. However, in the present study, the temperature for anatase-to-rutile transformation is as high as 1100°C, which indicates that these samples are promising to be used in hyperthermal situations.

## Evolution of the Morphology

The SEM images of the precursor $TiOF_2$ is shown in **Figure 2**. It can be clearly observed that these $TiOF_2$ nanoparticles are in cubic shape and relatively monodispersed (**Figure 2a**), which is consistent with the reported literatures (Chen et al., 2012; Wang

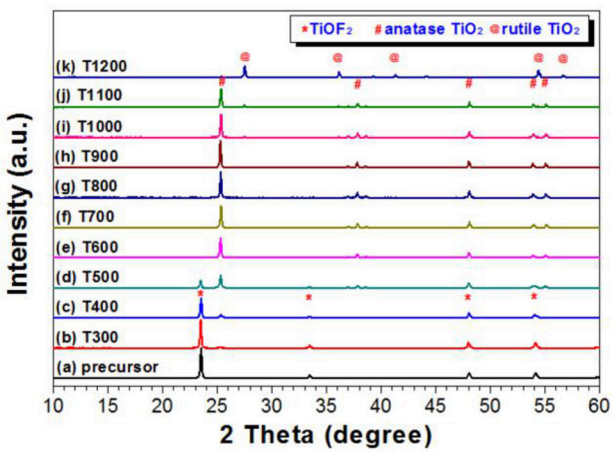


**FIGURE 1 |** XRD patterns of the photocatalysts calcined at different temperatures.

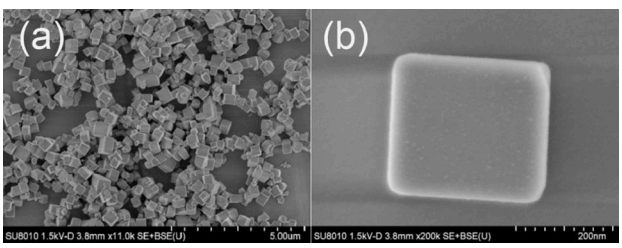


**FIGURE 2 |** SEM images of the precursor $TiOF_2$ at low **(a)** and high magnification **(b)**.

et al., 2012). From the high resolution SEM image shown in **Figure 2b**, we can estimate that the sidelength of the $TiOF_2$ cube is about 250 nm.

After calcination of the precursor $TiOF_2$ at 300°C, the morphology of the resulted sample (T300) almost keeps unchanged (SEM image not shown here). However, some nanoboxes with hollow interiors can be clearly seen from the SEM image of T400 sample (**Figure 3a**). These anatase $TiO_2$ hollow nanoboxes ($TiO_2$-HNBs) assemble from $TiO_2$ nanosheets ($TiO_2$-NSs) with exposed high energy (001) facets (Wen et al., 2011). The thickness of the $TiO_2$-NSs is about 30 nm. It has been proven that high energy $TiO_2$ nanosheets with exposed (001) facets can be prepared by using fluoride ions as shape-directing reagent (Yang et al., 2008; Lv et al., 2012). Then, it is not hard to understand the formation of high energy $TiO_2$-NSs during calcination of $TiOF_2$, a kind of fluorine-containing materials.

Since the sidelength of the obtained $TiO_2$-HNBs is similar as these precursor $TiOF_2$ cube, it is proposed that the formation of $TiO_2$-HNBs assembly from $TiO_2$-NSs is through a Ostwald Rippening process (Lou et al., 2008; Huang et al., 2013).

After calcination at 500°C, most of the $TiOF_2$ cubes transform into $TiO_2$-HNBs (**Figure 3c**). **Figure 3d** shows an enlarged SEM image of a broken $TiO_2$ hollow nanobox, from which we can see that the thickness of the $TiO_2$ nanosheet increases to about 50 nm, much thicker than that of T400 sample.

The structure of $TiO_2$-HNBs was further confirmed by the corresponding TEM image of T500 sample (**Figure 4a**), from which we can observe the presence of some erected $TiO_2$-NSs and a $TiOF_2$ cube that has not totally transformed into anatase $TiO_2$. This is consistent with the corresponding XRD characterization result (**Figure 1d**). From the side view HRTEM image of a discrete $TiO_2$-NS (**Figure 4b**), we can clearly see the lattice spacing of 0.235 nm that parallels to the top and bottom facets, which corresponds to the (001) planes of A-$TiO_2$ (Han et al., 2009). This confirms that the obtained $TiO_2$-HNBs are assembly from high energy $TiO_2$-NSs with exposed (001) facets (Wang et al., 2010).

When the calcination temperature increases to 600°C, we can see that almost all of the $TiO_2$-HNBs decompose into discrete $TiO_2$-NSs (**Figure 3e**). From the truncated biypramidal shape of a $TiO_2$ nanocrystals (**Figure 3f**), we can estimate that the thickness of the $TiO_2$-NSs is about 100 nm (T600 sample), which increases to ca. 150 nm for T700 sample (**Figures 3g,h**). Even calcined at 1100°C, some $TiO_2$ nanosheets still keep bipyramidal shape (decahedron) with exposed (001) and (101) facets (**Figures 3i,j**), further indicating the thermal stability of high energy $TiO_2$-NSs.

The bipyramidal shapes of $TiO_2$ nanostructures disappear (**Figures 3k,l**) when calcination of $TiOF_2$ cubes at 1200°C. This can be explained by the sintering of the sample due to phase transformation from A-$TiO_2$ to R-$TiO_2$ (**Figure 1**).

By comparing the morphologies of $TiO_2$-NSs from **Figure 3**, we can clearly see that heat treatment of $TiOF_2$ cubes only results in the growth of $TiO_2$ nanosheet along (001) direction. **Scheme 1** illustrates the morphology evolution and phase transformation of $TiOF_2$ cube during calcination.

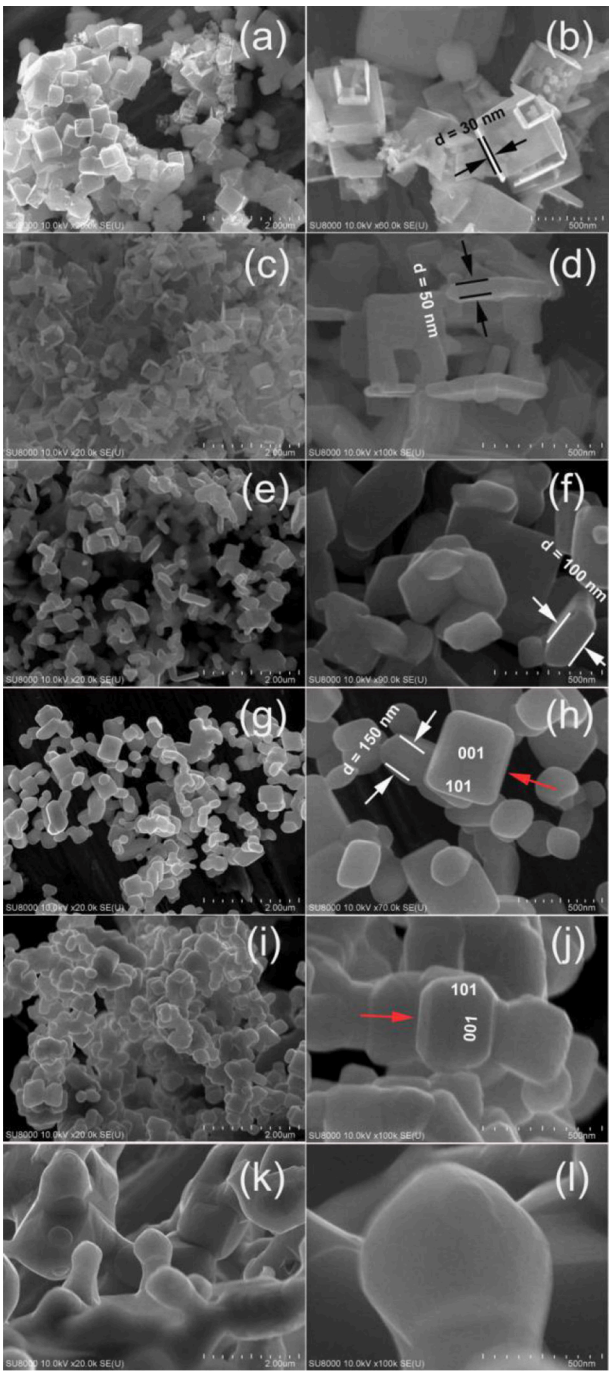


**FIGURE 3 |** Comparison of the SEM images for T400 **(a,b)**, T500 **(c,d)**, T600 **(e,f)**, T700 **(g,h)**, T1100 **(i,j),** and T1200 **(k,l)** samples.

## Uv-vis Absorption and FTIR Spectra

Light-harvesting ability plays a very important role on the photoreactivity of the photocatalyst (Li et al., 2017b). Therefore, we compared the UV-vis absorption spectra of the samples. It can be seen that from **Figure 5** that, when calcination temperature is below 1100°C, all samples possess similar absorption spectra

(**Figure 5**). The onset of the UV-vis absorption spectrum for T400 sample is at 389 nm, corresponding to a bangap of 3.19 eV. However, the absorption edge was obviously red-shifted for T1200 sample. The onset of the spectrum for T1200 sample begins at 424 nm, corresponding to a bandgap of 2.92 eV, which can be ascribed to the phase transformation (**Figure 1**).

**Figure 6** compares the FTIR spectra of the photocatalysts treated at different calcination temperature. From which, it can be seen that all samples exhibit strong absorption peaks cenerting at about 3,427, 1,628, 1,403, and 554 $cm^{-1}$. The peaks of 3,427 and 1,628 $cm^{-1}$ originate from the -OH groups/$H_2O$ due to the adsorption of moisture from the air, while the peaks centering at about 1403 and 554 $cm^{-1}$ originate from the vibration of

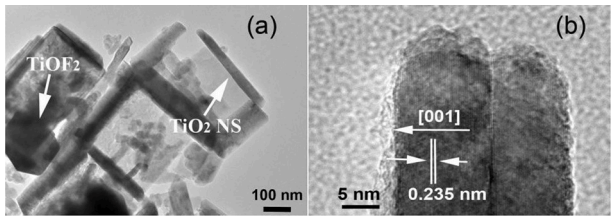


**FIGURE 4 |** TEM image **(a)** and high-resolution TEM image **(b)** of T500 sample, arrows in **(a)** indicating the presence of $TiOF_2$ cube and $TiO_2$ nanosheet ($TiO_2$-NS).

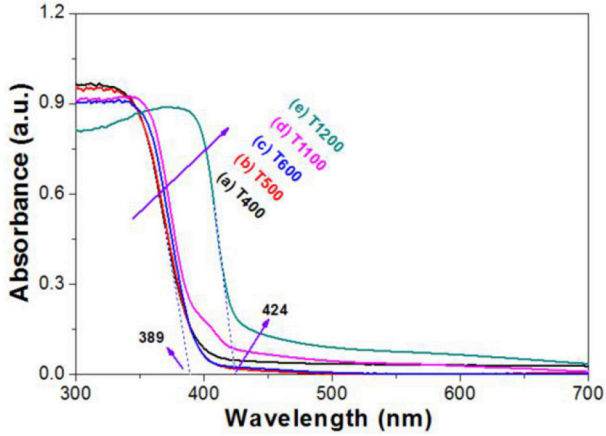


**FIGURE 5 |** UV-vis absorption spectra of the photocatalysts.

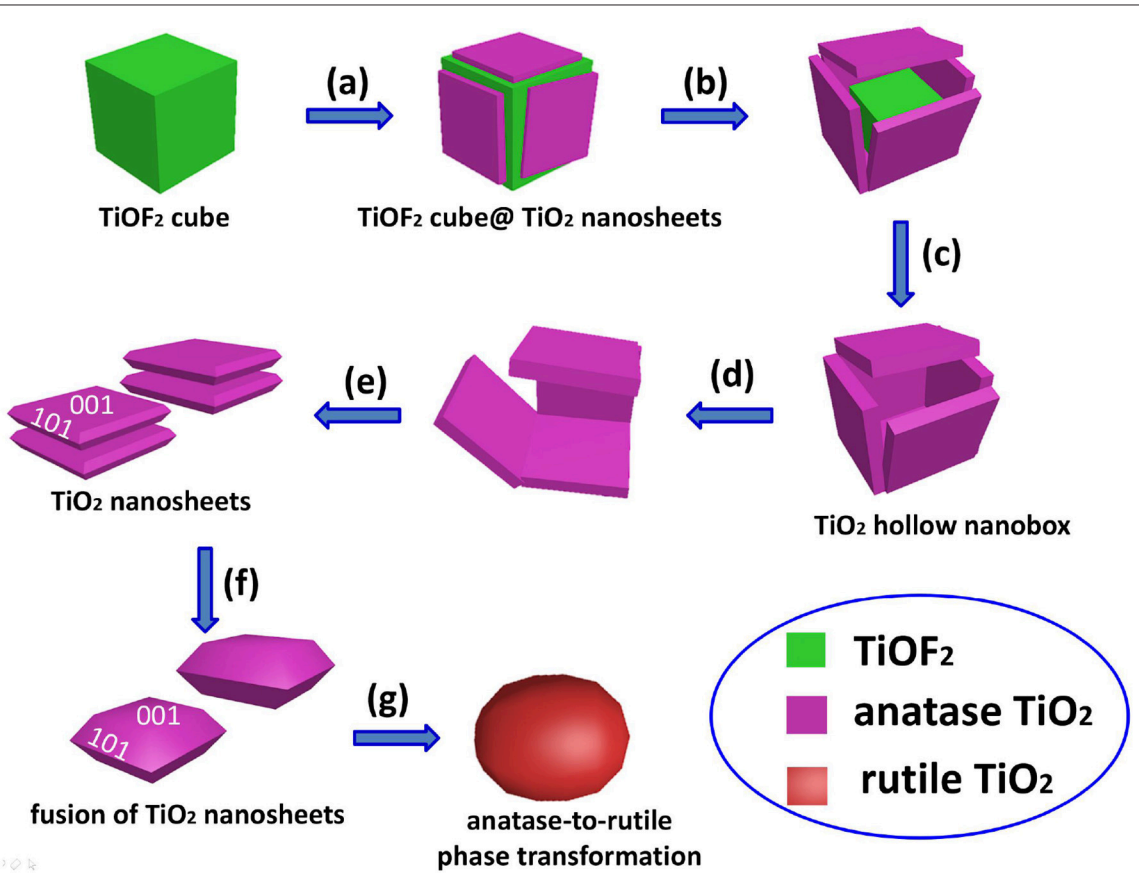


**SCHEME 1 |** Morphology evolution and phase transformation of $TiOF_2$ cube during calcination at different temperatures: **(a)** 300°C, **(b)** 400°C, **(c)** 500°C, **(d)** 600°C, **(e)** 700°C, **(f)** 1100°C, and **(g)** 1200°C.

Ti-O and O-Ti-O. Carefully view shows that there is a strong absorption peak at 978 $cm^{-1}$, which decreases with increasing in the calcination temperature. This peak was attributed to the vibration of Ti-F bond of $TiOF_2$. When calcination temperature increases to 600°C, the vibration of Ti-F disappears because of the complete phase transformation of $TiOF_2$-to-anatase $TiO_2$ (**Figure 1**; Zhao et al., 2018).

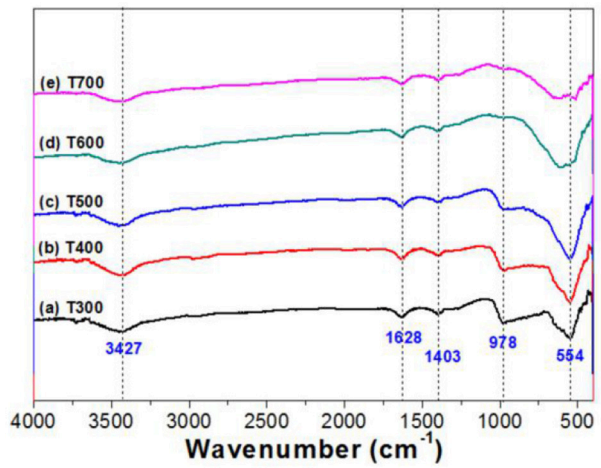


**FIGURE 6 |** FTIR spectra of the photocatalysts.

## Analysis of XPS Spectrum

**Figure 7**A compares the XPS survey spectra of photocatalysts for T400, T500, and T600 photocatalysts. From which, it can be observed that the XPS spectra are similar. All these samples contain titanium (Ti), oxygen (O), fluorine (F), and carbon (C) elements. The C element originates from the adventitious hydrocarbon from the XPS instrument itself. We can also be clearly see that the peak intensity of F element tends to decrease with increasing the calcination temperature from 400 to 600°C. The atomic ratios of F:Ti were determined to be 1.19 for T400 sample, 0.50 for T500 sample, and 0.17 for T600 sample, respectively. The steady decrease in F content with increase in the calcination is because of the $TiOF_2$ to A-$TiO_2$ phase transformation (**Figure 1** and Equation 1), and the removal of adsorbed fluoride ions on the surface of A-$TiO_2$.

**Figures 7B,C** show the high resolution XPS spectra in Ti 2p and O 1s regions, respectively. It can be seen that, both the binding energies for Ti 2p and O 1s of the samples steady decrease with increasing the calcination temperature. This is attributed to the $TiOF_2$-to-$TiO_2$ phase transformation (**Figure 1** and Equation 1), and the formation of oxygen vacancy due to

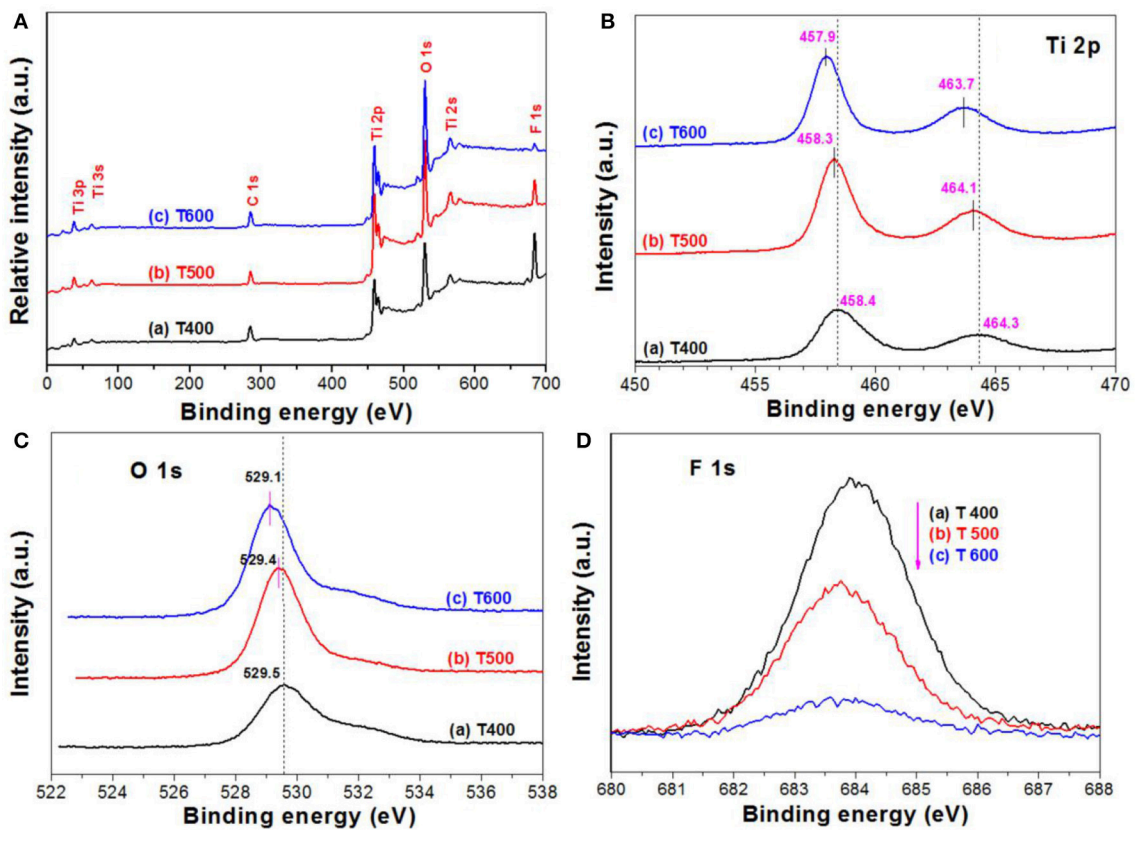


**FIGURE 7 |** XPS survey spectra of the photocatalysts **(A)**, and the corresponding high resolution XPS spectra in Ti 2p **(B)**, O 1s **(C),** and F 1s **(D)** regions, respectively.

the removal of surface adsorbed fluoride ions over $TiO_2$ upon calcination (Lv et al., 2011). It has been accepted that almost all of the fluoride ions adsorbed on the surface of high energy $TiO_2$ nanosheets can be removed after calcination at 500°C.

The F 1s binding energy peak centering at about 684 eV (**Figure 7D**) is designated to the surface fluoride (Ti-F). No peak with binding energy of about 688.5 eV, corresponding to the lattice $F^-$ of $TiO_2$, is found in all the photocatalysts, indicating that calcination of $TiOF_2$ cannot results in the doping of fluorine into anatase $TiO_2$ (Yu et al., 2002). We can also clearly see that the peak intensity of F 1s steady decreases with increasing the calcination temperature, this can be attributed to the heat-induced phase transformation from $TiOF_2$ to A-$TiO_2$ and the desorption of surface adsorbed fluoride ions (Yang et al., 2008).

## Photocatalytic Oxidation of Acetone

Photocatalytic oxidation of acetone was used to monitor the photoreactivity of the prepared photocatalyst. The reaction for the photocatalytic oxidation of acetone is as follows (Equation 2).

$$(CH_3)_2CO + 4O_2 = 3CO_2 + 3H_2O \quad (2)$$

**Figure 8A** compares the relative photoreactivity of the photocatalyst by calculation the decomposed acetone within 2 h. It was found that the photocatalytic activity of the precursor $TiOF_2$ can be neglected (only 4.0 ppm acetone was decomposed). The poor photocatalytic activity of $TiOF_2$ is possibly due to its easy recombination of photo-generated carriers.

The photocatalytic activity of the photocatalyst increases with increase in the calcination temperature from 300°C (12.8 ppm) to 500°C (102.5 ppm), which is due to the production of A-$TiO_2$. When further increase in the heat temperature from 600°C (94.6 ppm) to 1100°C (25.4 ppm), the photocatalytic activity of the photocatalyst steady decreases, possibly due to the decreased specific surface area (**Table 1**). Only 5.9 ppm of acetone was found to decompose when T1200 sample is used as photocatalyst. This is because of the complete A-$TiO_2$ to R-$TiO_2$ phase transformation (**Figure 1**) and smallest BET surface area (0.4 $m^2g^{-1}$).

Reusability of the photocatalyst is also important from the viewpoint of the practical applications (Liu et al., 2010). Therefore, we monitored the recycling use of T500 sample for 5 times in acetone oxidation (**Figure 8B**). It can be seen that no obvious reactivity decrease was observed for T500 sample even continual use for 5 times, indicating that T500 sample is potential to be used in practical applications.

## Mechanism

The value of photocurrent is usually used to evaluate the ability to generate and transfer of charge carriers for illuminated semiconductor photocatalyst (Cheng et al., 2018; Huang et al., 2018). The photocurrent of the prepared photocatalyst was therefore tested for several on-off cycles (**Figure 9**). It can be

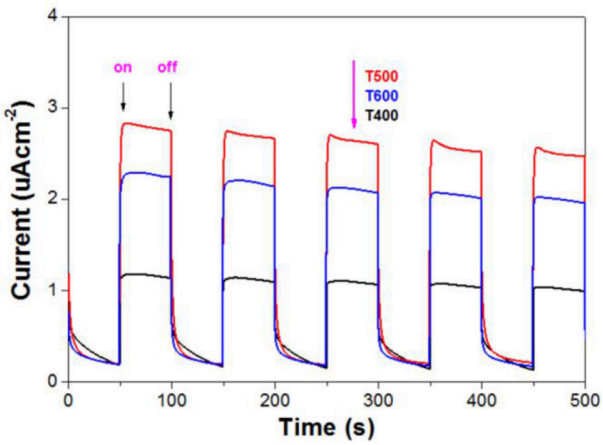


**FIGURE 9 |** Photocurrents of the photocatalysts.

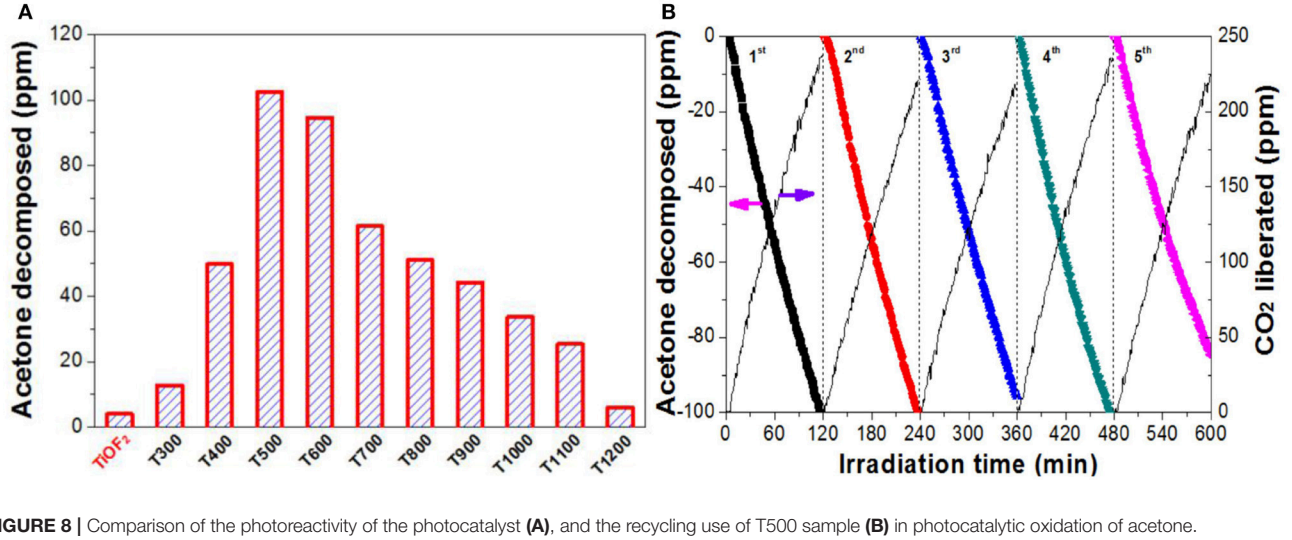


**FIGURE 8 |** Comparison of the photoreactivity of the photocatalyst **(A)**, and the recycling use of T500 sample **(B)** in photocatalytic oxidation of acetone.

seen that, when irradiation of the $TiO_2$ film electrodes, obvious prompt photocurrent signals are produced, which exhibit good reproducibility. When the lamp is turned off, the photocurrent value for all the $TiO_2$ film electrodes are instantaneously close to zero. We can also see, with increasing the calcination temperature from 400 to 600°C, the photocurrent of the photocatalyst increases first and then decreases. The photocurrent of T500 sample is the as high as 2.8 uAcm$^{-2}$, which is much higher than that of T400 (1.1 uAcm$^{-2}$) and T600 (2.3 uAcm$^{-2}$) samples. The photoreactivity of semiconductor photocatalyst is closely related to the efficiency of the separation of the photo-generated electron-hole pairs (Fu et al., 2008). So it is safe to predict that the photoreactivity of T500 is higher than that of T400 and T600 samples, which keeps in line with the experimental results (**Figure 8**).

It has been accepted that fluoride ions show strong affinity to titanium (Equation 3), and the photoreactivity of $TiO_2$ nanocrystals can be obviously improved after the introduction of surface fluorination (Minero et al., 2000; Xu et al., 2007; Cheng et al., 2008). According to the study of Yu et al., the difference in surface energy makes the photo-generated electrons and holes migrate to (101) and (001) facets, respectively (Yu et al., 2014). The CB electrons aggregated in (101) facets are captured by surface adsorbed oxygen to produce super oxygen radicals ($O_2^{\cdot-}$), while the VB holes aggregated on the (001)facets are transfer into hydroxyl radicals (·OH). Both $O_2^{\cdot-}$ and ·OH are important reactive oxygen species (ROSs) for the degradation of organics. When compared with pristine $TiO_2$, surface fluorination of $TiO_2$ changes the state of the formed hydroxyl radicals from surface bounded ·OH radicals (Equation 6) to mobile ·OH radicals ($\cdot OH_{free}$). This is because the displacement of fluoride to surface $OH^-$ groups (Equation 3) induces the direct oxidization solvent water by holes (Equation 7).

$$\equiv Ti - OH + F^- \rightarrow \equiv Ti - F + OH^- \quad (3)$$

$$TiO_2 + hv \rightarrow TiO_2\,(h^+ \cdots e^-) \quad (4)$$

$$O_2 + e^- \rightarrow O_2^{\cdot-} \quad (5)$$

$$\equiv Ti - OH + h^+ \rightarrow \equiv Ti\cdots OH \quad (6)$$

$$\equiv Ti - F + H_2O + h^+ \rightarrow \equiv Ti - F + \cdot OH_{free} \quad (7)$$

As free ·OH radical are more active than surface bounded ·OH radicals, the oxidation of acetone into $CO_2$ and $H_2O$ is greatly enhanced due to the attacks of super oxygen radicals and free ·OH radicals (Equation 8). The proposed mechanism for the enhanced photoreactivity of surface fluorinated $TiO_2$ nanosheet toward acetone oxidation is shown in **Scheme 2**.

$$C_3H_6O + O_2^{\cdot-}/\cdot OH_{free} \rightarrow CO_2 + H_2O \quad (8)$$

Recently, significantly growing interest has been devoted to studying of hierarchical nanostructures due to their unique properties and widespread potential applications (Lou et al., 2008). For example, when compared with solid spheres, $TiO_2$ hollow spheres usually shows much higher photocatalytic activity mainly because they possess better light-harvesting ability (Li et al., 2009). In the present study, the hierarchically structured

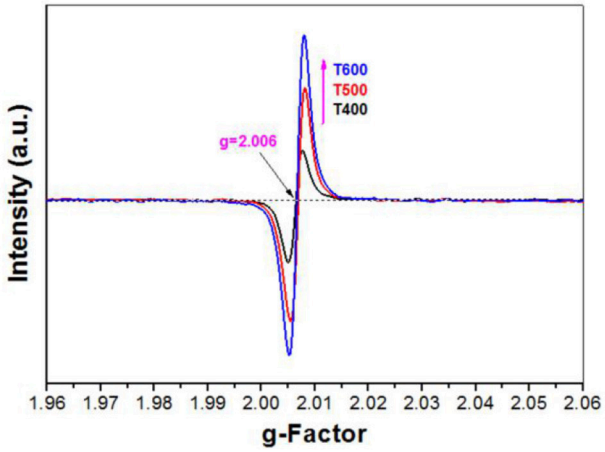


**FIGURE 10 |** EPR spectra of the photocatalysts.

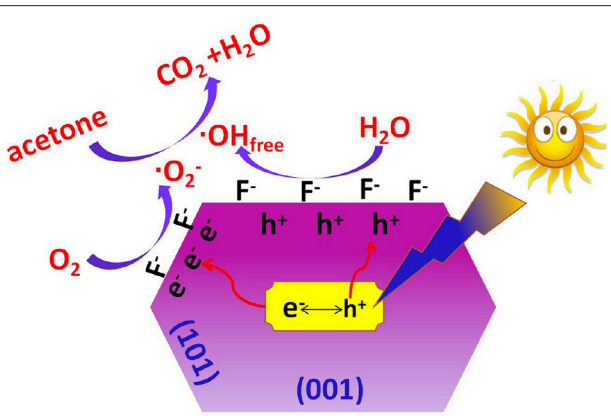


**SCHEME 2 |** Proposed mechanism for the enhanced photocatalytic activity of surface fluorinated TiO2 nanosheets with exposed high energy (001) facets toward acetone oxidation.

T500 sample, that is $TiO_2$ hollow nanobox assembly from $TiO_2$ nanosheets should also benefit the use of light (**Figure 5**), enhancing the photoreactivity.

However, the photoreactivity of $TiO_2$-NSs steady decrease with increase in the calcination temperature from 500 to 1100°C due to the collapse of the hierarchical $TiO_2$ hollow nanobox and the removal of surface adsorbed fluorine, leaving surface oxygen vacancy (**Figure 8**; Cheng et al., 2018).

$$\equiv Ti - F + heat \rightarrow \equiv Ti - \square \quad (9)$$

The formation of surface oxygen vacancy was proved by electron paramagnetic resonance (EPR) technique. It was found that the signal intensity for oxygen vacancy of the photocatalyst increases with increase in the calcination temperature from 400 to 600°C (**Figure 10**) due to the heat-induced desorption of

surface adsorbed fluoride ions (Equation 9).

$$\equiv \mathrm{Ti-OH} + \mathrm{HO-Ti} \equiv \rightarrow \equiv \mathrm{Ti-O-Ti} \equiv + \mathrm{H_2O} \quad (10)$$

$$\equiv \mathrm{Ti-\square} + \mathrm{\square - Ti} \equiv \rightarrow \text{ no reaction} \quad (11)$$

It was believed that only when the crystalline size of the nanocrystal is larger than a critical size can phase transformation begin (Padmanabhan et al., 2007; Periyat et al., 2008, 2009). Therefore, the growth of $TiO_2$ nanocrystal is a prerequisite before the phase transformation of A-$TiO_2$ to R-$TiO_2$. The growth of pristine $TiO_2$ nanocrystal is relatively easy by formation of =Ti-O-Ti= chain between two neighboring $TiO_2$ nanoparticles (Equation 10). However, the growth of the =Ti-O-Ti= chain is prevented due to the formation of surface oxygen vacancy (Equation 11). Only when the lattice oxygen is diffused from the bulk to the surface of $TiO_2$ nanosheet with oxygen vacancy at high temperaure can the fusion of neighboring $TiO_2$-NSs become possible (Lv et al., 2011). Therefore, it is not hard to understand the super thermal stability of $TiO_2$-NSs prepared by calcination of $TiOF_2$ cubes.

After the removal of surface adsorbed fluoride ions by calcination, these $TiO_2$-NSs prefer to aggregate and grow along (001) direction to reduce the high surface energy (Lv et al., 2011). Then we can clearly observe the steady increase in the thickness of $TiO_2$-NSs (**Figure 3**).

## CONCLUSIONS

$TiO_2$ nanosheets with high thermal stability were prepared by calcination of $TiOF_2$ cubes. The anatase-to-rutile phase transformation temperature reaches as high as 1100°C. 500°C-calcined sample shows the highest photoreactivity toward acetone oxidation due to the surface fluorination. The high thermal stability of $TiO_2$ nanosheets is ascribed to the introduction of surface oxygen vacancy after removal of the surface adsorbed fluoride ions, which prevents the growth of $TiO_2$ nanosheets. The present study provide a novel way in design of thermally stable materials.

## AUTHOR CONTRIBUTIONS

TS and YD performed the experiments. KL planned the project, designed the experiments, and wrote the manuscript. ZH, QL and XL assisted in the analysis and interpretation of the data. ML revised the manuscript.

## ACKNOWLEDGMENTS

This work was supported by the National Natural Science Foundation of China (51672312, 21571192 and 21373275), the Science and Technology Program of Wuhan (2016010101010018) and Fundamental Research Funds for the Central Universities, South-Central University for Nationalities (CZT18016).

## REFERENCES

Chen, J. S., Tan, Y. L., Li, C. M., Cheah, Y. L., Luan, D., Madhavi, S., et al. (2010). Constructing hierarchical spheres from large ultrathin anatase $TiO_2$ nanosheets with nearly 100% exposed (001) facets for fast reversible lithium storage. *J. Am. Chem. Soc.* 132, 6124–6130. doi: 10.1021/ja100102y

Chen, L., Shen, L. F., Nie, P., Zhang, X. G., and Li, H. S. (2012). Facile hydrothermal synthesis of single crystalline $TiOF_2$ nanocubes and their phase transitions to $TiO_2$ hollow nanocages as anode materials for lithium-ion battery. *Electrochim. Acta* 62, 408–415. doi: 10.1016/j.electacta.2011.12.058

Cheng, J. S., Hu, Z., Lv, K. L., Wu, X. F., Li, Q., Li, Y. H., et al. (2018). Drastic promoting the visible photoreactivity of layered carbon nitride by polymerization of dicyandiamide at high pressure. *Appl. Catal. B* 232, 330–339. doi: 10.1016/j.apcatb.2018.03.066

Cheng, X. F., Leng, W. H., Liu, D. P., Xu, Y. M., Zhang, J. Q., and Cao, C. N. (2008). Electrochemical preparation and characterization of surface-fluorinated $TiO_2$ nanoporous film and its enhanced photoelectrochemical and photocatalytic properties. *J. Phys. Chem. C* 112, 8725–8734. doi: 10.1021/jp7097476

Cui, W., Li, J. Y., Cen, W. L., Sun, Y. J., Lee, S. C., and Dong, F. (2017). Steering the interlayer energy barrier and charge flow via bioriented transportation channels in g-C3N4: enhanced photocatalysis and reaction mechanism. *J. Catal.* 352, 351–360. doi: 10.1016/j.jcat.2017.05.017

Fu, H. B., Xu, T. G., Zhu, S. B., and Zhu, Y. F. (2008). Photocorrosion inhibition and enhancement of photocatalytic activity for ZnO via hybridization with $C_{60}$. *Environ. Sci. Technol.* 42, 8064–8069. doi: 10.1021/es801484x

Han, X. G., Kuang, Q., Jin, M. S., Xie, Z. X., and Zheng, L. S. (2009). Synthesis of titania nanosheets with a high percentage of exposed (001) facets and related photocatalytic properties. *J. Am. Chem. Soc.* 131, 3152–3153. doi: 10.1021/ja8092373

Huang, T. T., Li, Y. H., Wu, X. F., Lv, K. L., Li, Q., Li, M., et al. (2018). In-situ transformation of $Bi_2WO_6$ to highly photoreactive $Bi_2WO_6$@$Bi_2S_3$ nanoplate *via* ion exchange. *Chin. J. Catal.* 39, 718–727. doi: 10.1016/S1872-2067(17)62913-9

Huang, Z. A., Wang, Z. Y., Lv, K. L., Zheng, Y., and Deng, K. J. (2013). Transformation of $TiOF_2$ cube to a hollow nanobox assembly from anatase $TiO_2$ nanosheets with exposed {001} facets via solvothermal strategy. *ACS Appl. Mater. Interfaces* 5, 8663–8669. doi: 10.1021/am4023048

Lan, J. F., Wu, X. F., Lv, K. L., Si, L. L., and Deng, K. J. (2015). Fabrication of $TiO_2$ hollow microspheres using $K_3PW_{12}O_{40}$ as template. *Chin. J. Catal.* 36, 2237–2243. doi: 10.1016/S1872-2067(15)60987-1

Li, X. F., Lv, K. L., Deng, K. J., Tang, J. F., Su, R., Sun, J., et al. (2009). Synthesis and characterization of ZnO and $TiO_2$ hollow spheres with enhanced photoreactivity. *Mater. Sci. Eng. B* 158, 40–47. doi: 10.1016/j.mseb.2008.12.036

Li, X., Yu, J. G., and Jaroniec, M. (2016). Hierarchical photocatalysts. *Chem. Soc. Rev.* 45, 2603–2636. doi: 10.1039/C5CS00838G

Li, Y. H., Lv, K. L., Ho, W. K., Dong, F., Wu, X. F., and Xia, Y. (2017a). Hybridization of rutile $TiO_2$ ($rTiO_2$) with g-$C_3N_4$ quantum dots (CN QDs): an efficient visible-light-driven Z-scheme hybridized photocatalyst. *Appl. Catal. B* 202, 611–619. doi: 10.1016/j.apcatb.2016.09.055

Li, Y. H., Lv, K. L., Ho, W. K., Zhao, Z. W., and Yu, H. (2017b). Enhanced visible-light photo-oxidation of nitric oxide using bismuth-coupled graphitic carbon nitride composite heterostructures. *Chin. J. Catal.* 38, 321–329. doi: 10.1016/S1872-2067(16)62573-1

Li, Y. H., Wu, X. F., Ho, W. K., Lv, K. L., Li, Q., Li, M., et al. (2018). Graphene-induced formation of visible-light-responsive $SnO_2$-$Zn_2SnO_4$ Z-scheme photocatalyst with surface vacancy for the enhanced photoreactivity towards NO and acetone oxidation. *Chem. Eng. J.* 336, 200–210. doi: 10.1016/j.cej.2017.11.045

Liang, L., Li, K. N., Lv, K. L., Ho, W. K., and Duan, Y. Y. (2017). Highly photoreactive $TiO_2$ hollow microspheres with super thermal stability for acetone oxidation. *Chin. J. Catal.* 38, 2085–2093. doi: 10.1016/S1872-2067(17)62952-8

Lin, S., Sun, S. Y., Shen, K. X., Tan, D. Y., Zhang, H. P., Dong, F. Q., et al. (2018a). Photocatalytic microreactors based on nano TiO2-containing clay colloidosomes. *Appl. Clay Sci.* doi: 10.1016/j.clay.2017.08.022. [Epub ahead of print].

Lin, S., Sun, S. Y., Wang, K., Shen, K. X., Ma, B. B., Ren, Y. Q., et al. (2018b). Bioinspired design of alcohol dehydrogenase@nano $TiO_2$ microreactors for sustainable cycling of $NAD^+$/NADH coenzyme. *Nanomaterials* 8, 1–9. doi: 10.3390/nano8020127

Liu, Y., Chen, L. F., Hu, J. C., Li, J. L., and Richards, R. (2010). $TiO_2$ nanoflakes modified with gold nanoparticles as photocatalysts with high activity and durability under near UV irradiation. *J. Phys. Chem. C* 114, 1641–1645. doi: 10.1021/jp910500c

Lou, X. W., Archer, L. A., and Yang, Z. C. (2008). Hollow micro-/nanostructures: synthesis and applications. *Adv. Mater. Weinheim.* 20, 3987–4019. doi: 10.1002/adma.200800854

Lv, K. L., Cheng, B., Yu, J. G., and Liu, G. (2012). Fluorine ions-mediated morphology control of anatase $TiO_2$ with enhanced photocatalytic activity. *Phys. Chem. Chem. Phys.* 14, 5349–5362. doi: 10.1039/c2cp23461k

Lv, K. L., Xiang, Q. J., and Yu, J. G. (2011). Effect of calcination temperature on morphology and photocatalytic activity of anatase $TiO_2$ nanosheets with exposed {001} facets. *Appl. Catal. B.* 104, 275–281. doi: 10.1016/j.apcatb.2011.03.019

Minero, C., Mariella, G., Maurino, V., and Pelizzetti, E. (2000). Photocatalytic transformation of organic compounds in the presence of inorganic anions. 1. Hydroxyl-mediated and direct electron-transfer reactions of phenol on a titanium dioxide-fluoride system. *Langmuir.* 16, 2632–2641. doi: 10.1021/la9903301

Padmanabhan, S. C., Pillai, S. C., Colreavy, J., Balakrishnan, S., McCormack, D. E., Perova, T. S., et al. (2007). A simple sol-gel processing for the development of high-temperature stable photoactive anatase titania. *Chem. Mater.* 19, 4474–4481. doi: 10.1021/cm070980n

Periyat, P., McCormack, D. E., Hinder, S. J., and Pillai, S. C. (2009). One-pot synthesis of anionic (nitrogen) and cationic (sulfur) codoped high-temperature stable, visible light active, anatase photocatalysts. *J. Phys. Chem. C* 113, 3246–3253. doi: 10.1021/jp808444y

Periyat, P., Pillai, S. C., McCormack, D. E., Colreavy, J. C., and Hinder, S. J. (2008). Improved high-temperature stability and sun-light-driven photocatalytic activity of sulfur-doped anatase $TiO_2$. *J. Phys. Chem. C* 112, 7644–7652. doi: 10.1021/jp0774847

Qi, K. Z., Cheng, B., Yu, J. G., and Ho, W. K. (2017). A review on $TiO_2$-based Z-scheme photocatalysts. *Chin. J. Catal.* 38, 1936–1955. doi: 10.1016/S1872-2067(17)62962-0

Regmi, C., Joshi, B., Ray, S. K., Gyawali, G., and Pandey, R. P. (2018). Understanding mechanism of photocatalytic microbial decontamination of environmental wastewater. *Front. Chem.* 6:33. doi: 10.3389/fchem.2018.00033

Sajan, C. P., Wageh, S., Al-Ghamdi, A. A., Yu, J. G., and Cao, S. W. (2016). $TiO_2$ nanosheets with exposed {001} facets for photocatalytic applications. *Nano Res.* 9, 3–27. doi: 10.1007/s12274-015-0919-3

Wang, Q., Qin, Z. N., Chen, J., Ren, B. S., Chen, Q. F., Guo, Y. C., et al. (2016). Green synthesis of nickel species *in situ* modified hollow microsphere $TiO_2$ with enhanced photocatalytic activity. *Appl. Surf. Sci.* 364, 1–8. doi: 10.1016/j.apsusc.2015.12.033

Wang, X. F., Yu, R., Wang, K., Yang, G. Q., and Yu, H. G. (2015). Facile template-induced synthesis of Ag-modified $TiO_2$ hollow octahedra with high photocatalytic activity. *Chin. J. Catal.* 36, 2211–2218. doi: 10.1016/S1872-2067(15)60978-0

Wang, Z. Y., Huang, B. B., Dai, Y., Zhang, X. Y., Qin, X. Y., Li, Z., et al. (2012). Topotactic transformation of single-crystalline $TiOF_2$ nanocubes to ordered arranged 3D hierarchical $TiO_2$ nanoboxes. *CrystEngComm* 14, 4578–4581. doi: 10.1039/C2CE25271F

Wang, Z. Y., Lv, K. L., Wang, G. H., Deng, K. J., and Tang, D. G. (2010). Study on the shape control and photocatalytic activity of high-energy anatase titania. *Appl. Catal. B* 100, 378–385. doi: 10.1016/j.apcatb.2010.08.014

Wen, C. Z., Hu, Q. H., Guo, Y. N., Gong, X. Q., Qiao, S. Z., and Yang, H. G. (2011). From titanium oxydifluoride ($TiOF_2$) to titania ($TiO_2$): phase transition and non-metal doping with enhanced photocatalytic hydrogen ($H_2$) evolution properties. *Chem. Commun.* 47, 6138–6140. doi: 10.1039/c1cc10851d

Wen, J. Q., Li, X., Liu, W., Fang, Y. P., Xie, J., and Xu, Y. H. (2015). Photocatalysis fundamentals and surface modification of $TiO_2$ nanomaterials. *Chin. J. Catal.* 36, 2049–2070. doi: 10.1016/S1872-2067(15)60999-8

Xia, Y., Li, Q., Lv, K. L., and Li, M. (2017). Heterojunction construction between $TiO_2$ hollowsphere and $ZnIn_2S_4$ flower for photocatalysis application. *Appl. Surf. Sci.* 398, 81–88. doi: 10.1016/j.apsusc.2016.12.006

Xu, X., Sun, Y. F., Fan, Z. H., Zhao, D. Q., Xiong, S. M., Zhang, B. Y., et al. (2018). Mechanisms for·$O_2^-$ and·OH production on flowerlike $BiVO_4$ photocatalysis based on electron spin resonance. *Frontier in Chem.* 6:64. doi: 10.3389/fchem.2018.00064

Xu, Y. M., Lv, K. L., Xiong, Z. G., Leng, W. H., Liu, W. P. D., and Xue, X. J. (2007). Rate enhancement and rate inhibition of phenol degradation over irradiated anatase and rutile $TiO_2$ on the addition of NaF: new insight into the mechanism. *J. Phys. Chem. C* 111, 19024–19032. doi: 10.1021/jp076364w

Yang, H. G., Liu, G., Qiao, S. Z., Sun, C. H., Jin, Y. G., Smith, S. C., et al. (2009). Solvothermal synthesis and photoreactivity of anatase $TiO_2$ nanosheets with dominant {001} facets. *J. Am. Chem. Soc.* 131 4078–4083. doi: 10.1021/ja808790p

Yang, H. G., Sun, C. H., Qiao, S. Z., Zou, J., Liu, G., Smith, S. C., et al. (2008). Anatase $TiO_2$ single crystals with a large percentage of reactive facets. *Nature* 453, 638–641. doi: 10.1038/nature06964

Yu, J. C., Yu, J. G., Ho, W. K., Jiang, Z. T., and Zhang, L. Z. (2002). Effects of $F^-$ doping on the photocatalytic activity and microstructures of nanocrystalline $TiO_2$ powders. *Chem. Mater.* 14, 3808–3816. doi: 10.1021/cm020027c

Yu, J. G., Low, J. X., Xiao, W., Zhou, P., and Jaroniec, M. (2014). Enhanced photocatalytic $CO_2$-reduction activity of anatase $TiO_2$ by coexposed {001} and {101} facets. *J. Am. Chem. Soc.* 136, 8839–8842. doi: 10.1021/ja5044787

Zhao, X., Du, Y. T., Zhang, C. J., Tian, L. J., Li, X. F., Deng, K. J., et al. (2018). Enhanced visible photocatalytic activity of $TiO_2$ hollow boxes modified by methionine for RhB degradation and NO oxidation. *Chin. J. Catal.* 39, 736–746. doi: 10.1016/S1872-2067(18)63039-6

Zhu, X. B., Tu, X., Mei, D. H., Zheng, C. H., Zhou, J. S., Gao, X., et al. (2016). Investigation of hybrid plasma-catalytic removal of acetone over CuO/g-$Al_2O_3$ catalysts using response surface method. *Chemosphere* 155, 9–17. doi: 10.1016/j.chemosphere.2016.03.114

**Conflict of Interest Statement:** The authors declare that the research was conducted in the absence of any commercial or financial relationships that could be construed as a potential conflict of interest.